EFFECTIVE DRAG LAW FOR PARCEL-BASED APPROACHES - WHAT CAN WE LEARN FROM CFD-DEM?

Stefan Radl[1,2], Matthew Girardi[2], and Sankaran Sundaresan[2]

[1] Graz University of Technology, Institute for Process and Particle Engineering
Inffeldgasse 21a / II
e-mail: radl@tugraz.at

[2] Princeton University, Dept. of Chemical and Biological Engineering
The Engineering Quad, Princeton, NJ
mgirardi@princeton.edu, sundar@princeton.edu

Keywords: discrete element method, filtering, fluidized beds

Abstract. *Computational fluid dynamics (CFD) simulations of dense gas-particle flows are extremely challenging due to the formation of clusters. These structures reduce the effective drag on the suspended particles and hence are key for the prediction of the flow in and the performance of fluidized beds. Our group has established models for the effective drag and particle-phase stress via Euler-Euler (EE) simulations [1]. However, EE simulations become cumbersome when treating polydisperse particle systems. Here, we focus on an Euler-Lagrange (EL) approach, with the goal to establish a sophisticated filtered drag model for coarse-grid (i.e., incompletely resolved) EL-based simulations. First, we detail the effect of the grid resolution and the particle-scale (i.e., "microscopic") drag law on our results. Based on our computational data from fully resolved EL-based simulations, we construct a filtered drag model for a later use in coarser EL-based simulations. Our results highlight the significant effect of particle clustering on the average slip velocity between particles and fluid, and indicate how this clustering can be accounted for in incompletely resolved EL-based simulations.*

1   INTRODUCTION

There have been significant efforts within the last ten years to quantify the effect of particle clustering on the slip velocity between a fluid and a particle phase [1–6]. Clustering is typically accounted for by modifying the expression for the fluid-particle drag, and recently a modification of the particle-phase stresses has also been suggested [1]. These modified expressions for the drag (and stress) can be used in so-called "coarse-grid" simulations with a computational grid resolution larger than that of the characteristic cluster size. As the diameter of process vessels in many engineering applications is typically three orders of magnitude larger than the cluster size, coarse-grid simulations have to be used in industrial practice.

Most of the previous work on clustering in fluid-particle systems was based on the so-called two-fluid model (TFM), i.e., an EE-based model that treats the particle phase as a continuum. TFMs typically use the kinetic theory of granular flow (KTGF) to provide a closure for the particle-phase stress. The problem associated with most theories for KTGF is that they are based on the assumption of instantaneous particle-particle interactions and nearly elastic collisions. This limits the use of TFM to non-cohesive granular flows at low (particle) Mach numbers.

Simulations based on a Lagrangian treatment of the particle phase do not have the above limitations, but they are restricted to relatively small systems because the number of particles that can be tracked is limited. For systems with reactions on the surface of particles, or wet gas-particle systems, however, Lagrangian methods have significant advantages over TFM-based formulations. Similar to TFM-based simulations, the effect of particle clustering has already been taken into account in EL-based fluid-particle flow simulations [7–10]. However, the modification of the drag law in these previous studies was rather heuristic. For example, Helland and co-workers [11] propose the use of a second-order polynomial to describe the drag reduction at low particle volume fractions (i.e., below $\phi_p = 0.10$). Their model is parameterized with some experimental findings for dilute suspension, which clearly cannot accurately describe the complex phenomena observed in dense suspensions. An open question remains whether the same correction to the drag force should be used for Lagrangian and TFM-based simulations. Here, we use detailed EL-based simulations of gas-particle systems to generate, in contrast to postulate, an expression for a drag law that is able to correctly quantify the clustering effect.

2   GOVERNING EQUATIONS

We combine a solver for the incompressible Navier-Stokes equation [12] with a high-performance implementation [13] of the discrete element method (DEM), henceforth referred to as CFD-DEM [14]. In this approach, we track the center of each particle, its rotational position as well as its translational and angular velocity. We consider a large (i.e., $O(10^6)$) number of particles, and hence cannot resolve the details of the fluid flow around each individual particle. Consequently we solve the mass and momentum balance equations for a locally-averaged fluid velocity, and supply a "microscopic" drag law on the level of individual particles (see Chapter 2.3 for details). We supply a model for the contact force between particles to mimic the behavior of stiff, slightly inelastic particles (see Appendix A).

2.1   Fluid Phase

The mass and momentum balance equation for the fluid phase are:

$$\frac{\partial \left(\rho_f \phi_f \right)}{\partial t} + \nabla \cdot \left(\rho_f \phi_f \mathbf{u} \right) = 0 \tag{1}$$

$$\frac{\partial \left(\rho_f \phi_f \mathbf{u} \right)}{\partial t} + \nabla \cdot \left(\rho_f \phi_f \mathbf{u}\mathbf{u} \right) = -\phi_f \nabla p_f - \phi_f \nabla \cdot \boldsymbol{\tau}_f + \boldsymbol{\Phi} + \rho_f \phi_f \mathbf{g} \tag{2}$$

Here $\mathbf{g}$, ρ_f, ϕ_f, p_f, $\boldsymbol{\tau}_f$ and $\mathbf{u}$ are the gravitational acceleration, the fluid density, the fluid volume fraction, pressure, viscous stress tensor and (average) fluid velocity, respectively. $\boldsymbol{\Phi}$ is the specific coupling force exerted by the particle phase on the fluid phase (i.e., a force per unit volume of the gas-particle mixture) - in general, this term should include the drag, added mass, lift and history force contributions. However, for gas-particle flows considered here, the fluid-particle drag force contribution is the most significant one and all the other contributions are usually neglected. We also do not consider pseudo-turbulent motion in the fluid, and hence the fluid stress tensor $\boldsymbol{\tau}_f$ can be easily calculated from the rate of deformation of the fluid and a molecular viscosity μ_f of the fluid.

Because we are interested in the simulation of gas-particle flows in fully periodic boxes, we re-arrange the momentum equation, i.e., we split up the fluid pressure p_f into a dynamic and hydrostatic pressure:

$$\nabla p_f = \nabla p_{dyn} + \rho_{mix} \mathbf{g} . \tag{3}$$

Here, ρ_{mix} is the domain-averaged mixture density. By inserting above expression for the pressure gradient, we obtain a momentum balance equation with a modified term for the gravitational acceleration, and $\mathbf{u}$ and p_{dyn} as variables. We can now apply periodic boundary conditions for p_{dyn}, since the pressure gradient due to the weight of the gas-particle mixture is already taken into account via $\rho_{mix} \mathbf{g}$. Consequently, our flow is driven by a pressure gradient that is equal to the weight of the particles, and the total momentum of our gas-particle system remains constant except for small numerical errors, which are less than 1% of the total particle momentum in our simulations. Details of the numerical algorithm to solve the fluid-phase equations are summarized in Appendix A.

2.2 Particle Phase

The particle phase is assumed to consist of frictional, inelastic spheres. We use contact force models inspired by Luding [15], specifically the linear spring-dashpot model with frictional slider detailed by Radl et al. [13]. The acceleration of each particle is calculated via:

$$\mathbf{a} = \frac{\mathbf{f}_{cont,i}}{\rho_p V_{p,i}} + \frac{\beta_{p,i}}{\rho_p} \left(\mathbf{u}_i - \mathbf{v}_i \right) - \frac{1}{\rho_p} \nabla p_{f,i} + \mathbf{g} . \tag{4}$$

Here $\mathbf{f}_{cont,i}$, ρ_p, $\mathbf{v}_i$ and $V_{p,i}$ is the total contact force that acts on particle i, the particle density, the particle velocity, and the particle's volume, respectively. $\beta_{p,i}$ is a drag coefficient, for which a model equation is supplied in the next paragraph. The subscript i next to the fluid velocity $\mathbf{u}$ and the fluid pressure p_f indicates that these quantities are evaluated at the particle's center position.

2.3 Microscopic Drag Model

We model the fluid-particle interaction force $\mathbf{f}_d$ by a drag coefficient and the relative velocity between fluid and particle:

$$\mathbf{f}_{d,i} = V_{p,i}\,\beta_{p,i}\left(\mathbf{u}_i - \mathbf{v}_i\right). \tag{5}$$

Various models for the drag coefficient β_p exist, but most of them can be condensed to the following expression:

$$\beta_p = \frac{18\,\mu_f}{d_p{}^2}\left(1-\phi_p\right)\left[F_0\left(\phi_p\right)f\left(Re_p\right)+G_0\left(Re_p\right)\right]. \tag{6}$$

The term in the square brackets is typically denoted as F, and d_p and ϕ_p is the particle diameter and the particle volume fraction, respectively. Here Re_p is the particle Reynolds number:

$$Re_p = \frac{\phi_f\,\rho_f\,d_p\left|\mathbf{u}-\mathbf{v}\right|}{\mu_f}. \tag{7}$$

Three typical drag models are summarized in Table 1, and they are valid up to $Re_p = 1,000$. We have used the Wen-Yu [16] model, as well as the Beetstra et al. [17] model in our simulations. We also checked the effect of a fluctuating drag force [18] on our results, however, we found that the effect of such a fluctuation is small for the parameter space investigated by us. It would be natural to include a model for the hydrodynamic torque that the fluid exerts on the particles. We have tested such a torque model as suggested by Hölzer and Sommerfeld [19], but since the fluid density in our case is small, the effect of this torque was found to be negligible.

Drag Model	$F_0(\phi_p)$	$f(Re_p),\ G_0(Re_p)$
Wen-Yu [16]	$\left(1-\phi_p\right)^{-3.65}$	$f = 1+0.15Re_p{}^{0.687}$; $G_0 = 0$
Beetstra et al. [17]	$\dfrac{10\,\phi_p}{\left(1-\phi_p\right)^2}+$ $\left(1-\phi_p\right)^2\left(1+1.5\sqrt{\phi_p}\right)$	$f=1;$ $G_0 = \dfrac{0.413\,Re_p}{24\left(1-\phi_p\right)^2}\cdot$ $\left[\dfrac{\left(1-\phi_p\right)^{-1}+3\,\phi_p\left(1-\phi_p\right)+8.4\,\mathrm{Re}_p{}^{-0.343}}{1+10^{3\phi_p}\,Re_p{}^{-(1+4\phi_p)/2}}\right]$
Tenneti et al. [20]	$\dfrac{1+5.81\phi_p}{\left(1-\phi_p\right)^2}+0.48\dfrac{\phi_p{}^{1/3}}{\left(1-\phi_p\right)^3}$	$f=1;$ $G_0 = \dfrac{0.15Re_p{}^{0.687}}{\left(1-\phi_p\right)^2}+$ $+\phi_p{}^3\left(1-\phi_p\right)Re_p\left[0.95+\dfrac{0.61\phi_p{}^3}{\left(1-\phi_p\right)^2}\right]$

Table 1: Commonly used drag laws for gas-particle flow simulations.

3   CASE DESCRIPTION

We perform CFD-DEM simulations in a fully periodic domain with proportions 1x4x1 (*width* x *height* x *length,* see Figure 1, left panel). We considered a system size with a *width* = 53.3 d_p, as well as a *width* = 107 d_p, and varied the domain-averaged particle volume fraction from 0.02 to 0.50. This required us to track between $2.3 \cdot 10^4$ and $4.64 \cdot 10^6$ particles. Our system is characterized by a particle Reynolds number of 1.18, a particle-to-fluid density ratio of 1154, a particle Froude number of 65, and is equal to that used by Igci et al. [1].
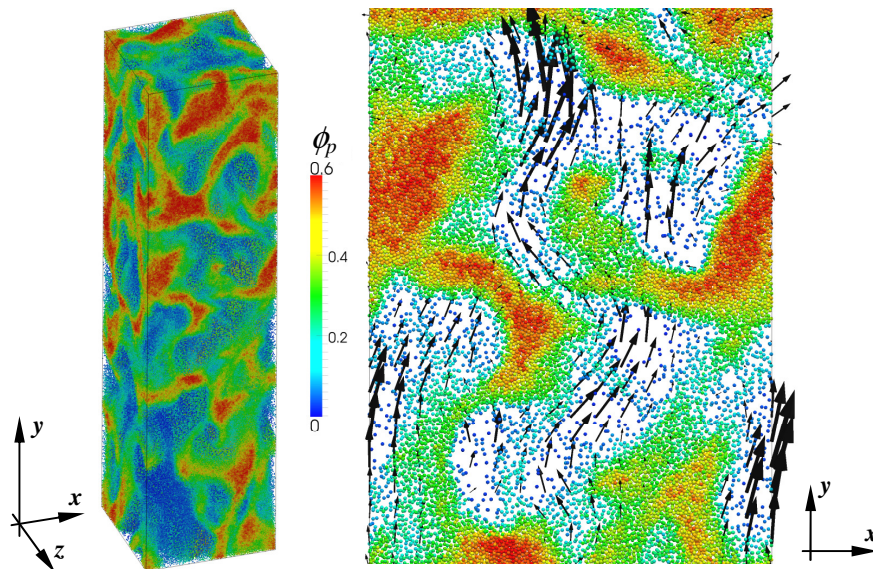
Figure 1: Particle volume fraction at the particle position and fluid flow field in a periodic domain simulation ($2.3 \cdot 10^6$ particles, $<\phi_p> = 0.25$, 107 x 427 x 107 d_p domain size; the right panel shows a small slice located at the front of the image on the left).

4   RESULTS

4.1   Averaged Slip Velocities and Filtered Drag Coefficient

We illustrate our filter strategy by defining a filtered slip velocity at the particle location. This slip velocity is calculated from a filtered fluid velocity and the velocity of a single particle:

$$\overline{\mathbf{u}}_{slip,i} = \left(\frac{\overline{\mathbf{u}_f \cdot \phi_f}}{\overline{\phi_f}} \right)_i - \mathbf{v}_i \tag{8}$$

Here the subscript i indicates that the filtered quantity is evaluated at the particle position, and the overbar refers to an average over a cubic filter region with length Δ_{filter}. In order to compare various numerical settings, it is useful to define a domain-averaged slip velocity

$$\left\langle \mathbf{u}_{slip} \right\rangle = \frac{\left\langle \mathbf{u}_f \, \phi_f \right\rangle}{\left\langle \phi_f \right\rangle} - \frac{\sum_{N_p} V_{p,i} \, \rho_p \, \mathbf{v}_i}{\sum_{N_p} V_{p,i} \, \rho_p} \, . \tag{9}$$

Here < > indicates averaging over the whole computational domain.

Similarly to the filtered slip, we define a filtered drag coefficient, which is essentially the ratio of the effective drag acting on a particle and the filtered slip velocity. In addition, we make use of the fact that in a coarse-grid simulation we will precisely know the filtered buoyancy term. Hence, we subtract this contribution from the filtered buoyancy force acting on the particle, and require adding this term later in coarse-grid simulation. Thus, we define the filtered drag coefficient in each spatial direction n as:

$$\overline{\beta}_{p,i,n} = \frac{1}{\overline{\mathbf{u}}_{slip,i,n}}\left[-\nabla p_{f,i} + \nabla \overline{p}_{f,i} + \beta_{p,i}\left(\mathbf{u}_i - \mathbf{v}_i\right)\right]_n \tag{10}$$

For our analysis below, we consider only the component of the filtered drag coefficient that is parallel to gravity (i.e., the y-component). The filtered slip velocity and drag coefficient are calculated for each particle, binned with respect to the filtered particle volume fraction (typically, we use 100 bins and collect between a few thousand and 10^7 samples per bin), and averaged over at least 20 dimensionless time units $t^* = t / (u_t / g)$. Averaging starts after the flow is developed, which is typically the case for $t^* > 15$.

4.2   Domain-Averaged Slip and the Effect of the Microscopic Drag Law

In order to assess the accuracy of the CFD-DEM approach for our gas-solid flow, we performed a grid dependency study for small to moderately dense particle concentrations. This study showed that all our results for $<\mathbf{u}_{slip}>$ (summarized in Table 2, data were time-averaged over at least 20 t^*) are within 3% and 5% for a domain average volume fraction of $<\phi_p> = 0.05$ and 0.25, respectively. For the case with the highest particle volume fraction (i.e., $<\phi_p> = 0.50$) we found that there are more substantial variations upon grid refinement. We conclude that this is due the formation of bubbles (see Figure 2) which, depending on the fluid grid resolution, can have different sizes. The large bubbles observed at the finest fluid grid resolution (shown in Figure 2) lead to instantaneous vertical particle velocities in the order of the terminal settling velocity. These large bubbles were not seen on coarser fluid grids. We hence have excluded this data from our results for the filtered drag coefficient.

$<\phi_p>$	homogeneous suspension $<\mathbf{u}_{slip,y}> / u_t$	CFD-DEM simulation $<\mathbf{u}_{slip,y}> / u_t$	$<\mathbf{u}_{slip,y}>_{CFD\text{-}DEM}$ / $<\mathbf{u}_{slip,y}>_{homogeneous}$
0.02	0.761	1.25	1.64
0.05	0.607	1.26	2.08
0.10	0.447	1.25	2.80
0.15	0.340	1.26	3.71
0.20	0.262	1.10	4.20
0.25	0.203	1.04	5.12
0.35	0.121	0.888	7.24
0.40	0.0931	0.639	6.86
0.50	0.0536	0.268	5.00

Table 2: Domain-averaged slip velocity in a periodic domain (Beetstra et al. drag law, 107 x 427 x 107 d_p domain size, $\Delta_{fluid} = 3.33\ d_p$).

Figure 3 illustrates the influence of the microscopic drag law on our statistics for the filtered slip velocity. Here we compare two microscopic drag laws, namely the Wen-Yu and the Beetstra et al. correlation, that differ quite significantly (i.e., roughly 40% for intermediate

volume fractions) from each other. In the left panel of Figure 3, our data on the dimensionless filtered slip velocity shows qualitatively similar trends, however, the (dimensionless) slip velocity is markedly different for the two drag laws (with an average difference of ca 30%). The results for the case with the higher microscopic drag (i.e., the Beetstra et al. model) yields a slip velocity closer to that of a homogeneous suspension, as expected. While there are quantitative differences for the filtered slip velocity, the filtered drag coefficients are in better agreement for both microscopic drag models, with significant differences only for $\bar{\phi}_p > \langle \phi_p \rangle$ (see Figure 3, right panel, the average difference is ca 6%). Clearly, the microscopic drag law has little influence on the normalized filtered drag coefficient. Hence, we focus in the following work exclusively on the drag formulation of Beetstra et al.
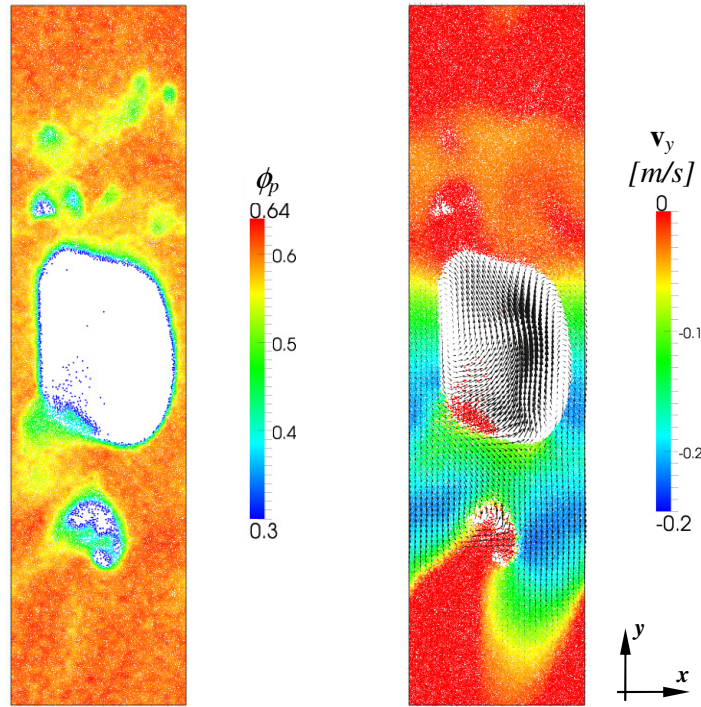

Figure 2: Particle volume fraction at the particle position (left panel), as well as the particles' vertical velocity and vectors indicating the fluid flow field (right panel) in a cross-section of a periodic domain simulation ($4.64 \cdot 10^6$ particles, $\langle \phi_p \rangle = 0.50$, $\Delta_{fluid} = 3.33\ d_p$, 107 x 427 x 107 d_p domain size; the reference velocity is $u_t = 0.232$ [m/s]).

4.3   Model for the Filtered Drag Coefficient in Euler-Lagrange Simulations

By combining results for simulations with $\langle \phi_p \rangle$ ranging from 0.02 to 0.40, we now construct a master curve for the normalized filtered drag coefficient (see Figure 4). We have also included a fit to our data (black lines in Figure 4), the former being of the form:

$$\frac{\bar{\beta}_p}{\beta_p} = 1 - f\left(F_f, \bar{\phi}_p\right) h\left(\bar{\phi}_p\right), \text{ with } f\left(F_f, \bar{\phi}_p\right) = \frac{F_f^{-1}}{a_{F_f}\left(\bar{\phi}_p\right) + sign\left(\bar{\phi}_p - \phi_{p,crit}\right) F_f^{-1}} \ . \tag{11}$$

Here $F_f = d_p / \Delta_{filt}$ is a dimensionless (inverse) filter size, and $a_{F_f}\left(\bar{\phi}_p\right)$ as well as $h\left(\bar{\phi}_p\right)$ are fitting functions to be published in a forthcoming paper. Note, the choice of d_p as the reference length for the dimensionless filter size is rather arbitrary, and hence does not make our results universally applicably to fluid-particle systems. However, for typical gas-particle flows with d_p and ρ_p close to 75 µm and 1500 kg/m³, respectively, this scaling will yield ac-

ceptable results. $\phi_{p,crit}$ is a critical particle volume fraction that marks the transition from $\bar{\beta}_p / \beta_p > 1$ for small $\bar{\phi}_p$ to $\bar{\beta}_p / \beta_p < 1$ for large $\bar{\phi}_p$.
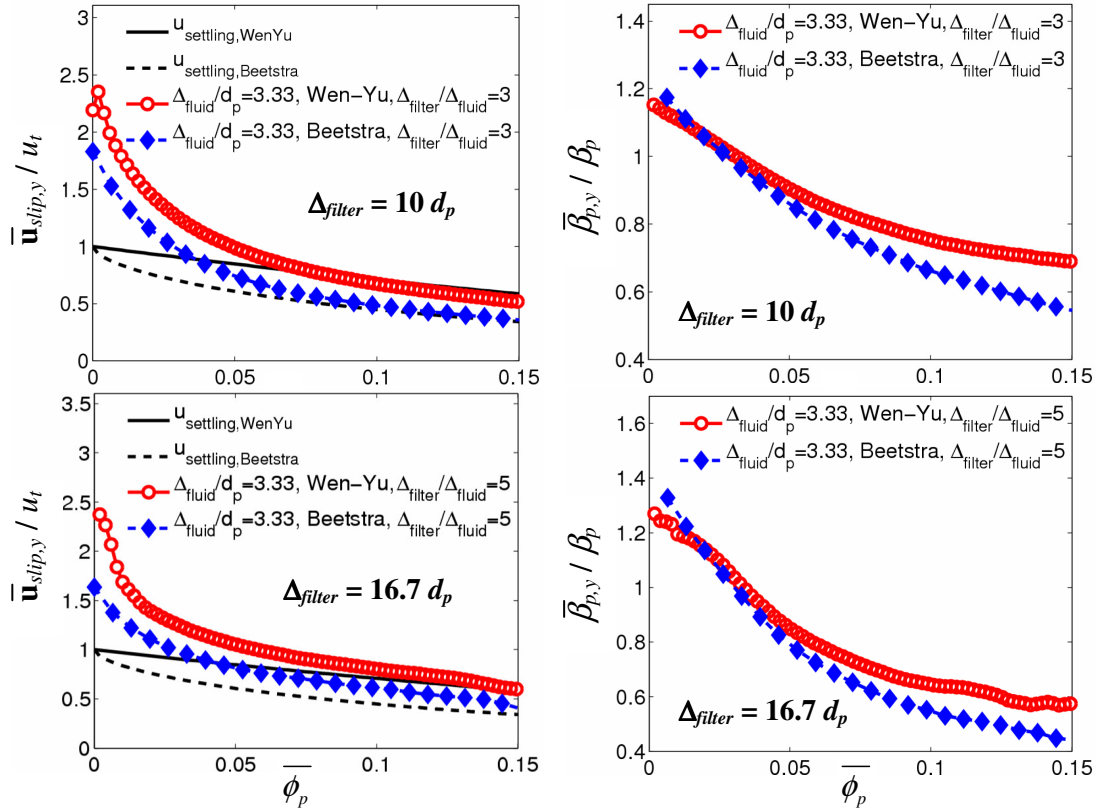

Figure 3: Normalized drag coefficient (left panel; black lines indicate the settling velocity of a homogeneous suspension) and slip velocity (right panel) for Wen-Yu and Beetstra drag model ($<\phi_p>$ = 0.05; 53 x 213 x 53 d_p domain; the top row shows data for Δ_{filter} = 10 d_p, and the bottom row for Δ_{filter} = 16.7 d_p).

As can be seen from Figure 4 and unlike previous work [1], we find that the filtered drag coefficient can exceed the microscopic drag coefficient at extremely low particle concentrations (see Figure 4, right panel). This is because in dilute regions, the fluid velocity experienced by individual particles is on average larger than the spatially-averaged (i.e., filtered) fluid velocity. We will explain this fact in greater detail in the following paragraph. For $\bar{\phi}_p$ ranging from $\phi_{p,crit}$ = 0.016 to ϕ_p = 0.60, we observe a significant decrease of the effective drag on individual particles (see Figure 4, left panel). Similar to previously published models, the effective drag decreases for increasing filter size. We observe already a strong decrease (i.e., -50%) of the drag at a filter size of 10 d_p. This is in contrast to the finding of Igci et al. [1], which report grid-insensitive results for their TFM simulations when choosing a grid resolution of 10 d_p. While the exact reason for this disagreement cannot be isolated, we speculate that this is due to the fact that (i) the small-scale clustering had only minor effects on the results of Igci et al. [1] as they used comparably large domains, and (ii) the inability of the TFM to accurately model structure formation at small scales and the resulting saturation of particle clustering upon grid refinement. Unfortunately, we cannot directly compare TFM- and CFD-DEM-based simulations in large enough boxes, because the latter would require extremely long computations. However, TFM-based simulations in boxes with the same size as used in this work show that TFMs behave poorly (i.e., predict significantly less clustering) than CFD-DEM-based models (data not shown).
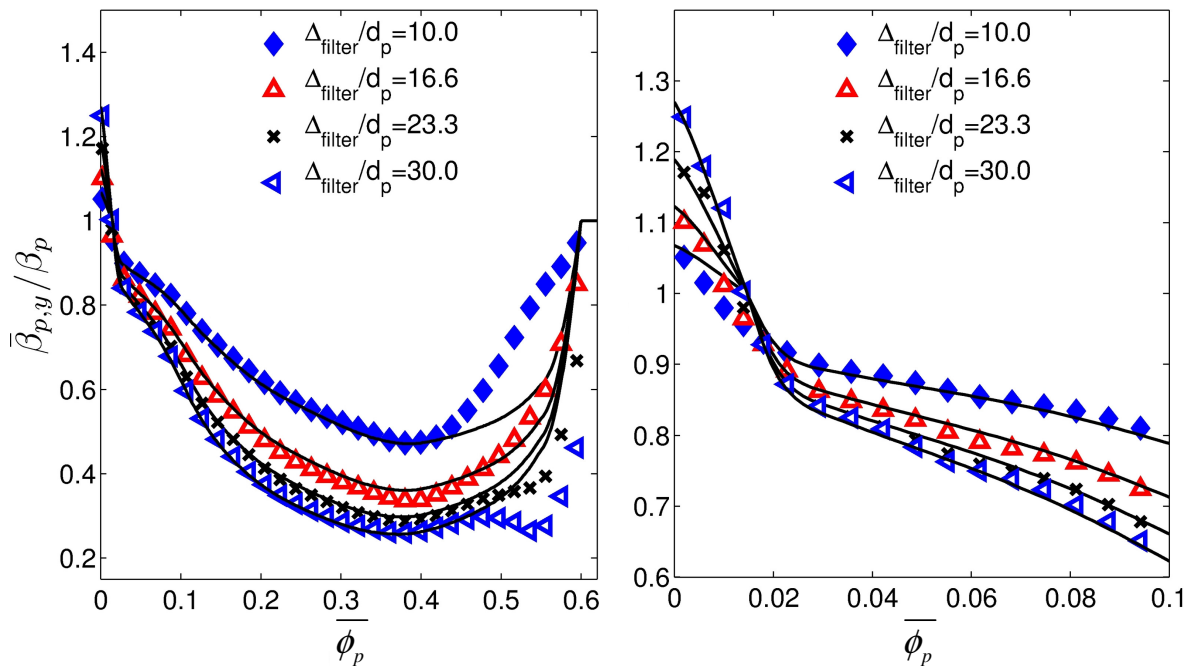
Figure 4: Dimensionless filtered drag coefficient for various filter sizes and volume fractions (symbols: data from CFD-DEM simulation; black lines: model prediction, i.e., Eqn. 11; the right panel shows the data for volume fractions below 0.10).
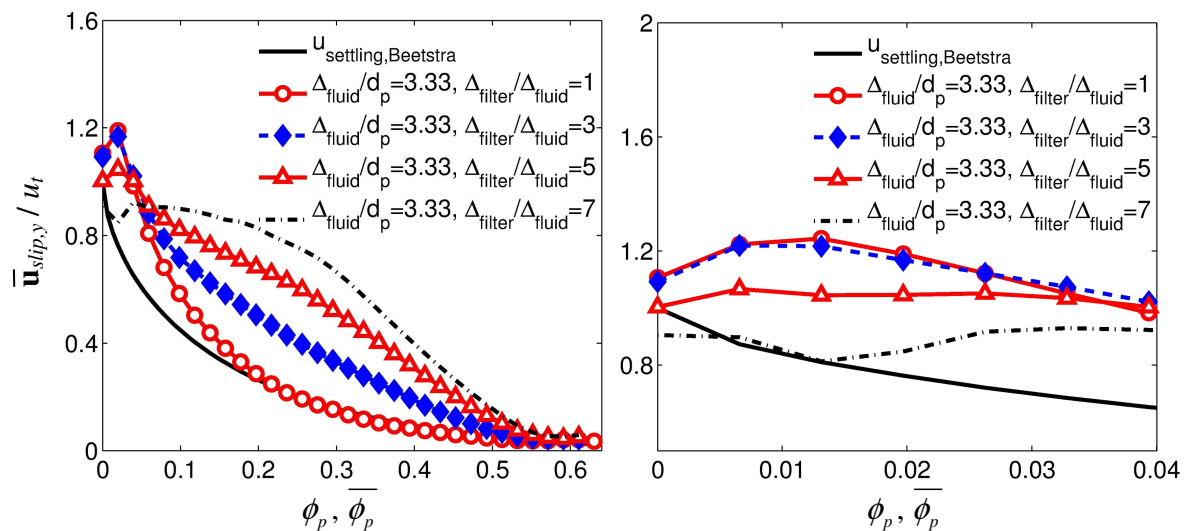

Figure 5: Dimensionless filtered slip velocity for various filter sizes (symbols and dash-dotted line) and slip velocity for a homogeneous suspension (solid line; Beetstra drag model, $<\phi_p> = 0.40$).

As already mentioned, at low particle volume fractions, there is an increase in the filtered drag coefficient. The origin of this fact is simple: particles in dilute regions are surrounded by regions of higher particle volume fraction. Consequently, the particle of interest (placed in the more dilute region of the filter region) will experience a higher local fluid velocity in the vertical direction compared to the average fluid velocity in the filter region (which includes also the denser regions with smaller slip). Thus, also the drag force on such a single particle is higher than one would expect from the average fluid velocity in the filter region. Hence, when calculating a filtered drag coefficient that is based on the force on the particle and the difference between the particle and the filtered fluid velocity in the filter region, one will obtain on average an effective drag coefficient for these particles that is larger than the microscopic

drag coefficient. To support our arguments, we show the filtered slip velocities for various filter sized and a domain-averaged volume fraction of $<\phi_p> = 0.40$ in Figure 5. As can be seen, the filtered slip velocity decreases with increasing filter size at low particle concentrations. In addition, we find that for simulations with $<\phi_p>$ smaller than 0.40 the filtered slip velocity does increase with increasing filter size, but still the normalized filtered drag coefficient is larger than unity in dilute regions. We argue that for these systems the slip velocity in the dilute region is (on average) between 2.0 and 2.4 times higher than the terminal settling velocity, and the filtered slip velocity decreases monotonically with increasing particle volume fraction (see Figure 3). This means that particles are strongly accelerated when moving from a moderately dense to a dilute region, which leads to the observed increase of the effective drag coefficient.

5   CONCLUSIONS

We outline an approach for constructing filtered drag models from CFD-DEM-based simulations in order to account for the clustering of particles. We use such an approach to construct an effective drag model for coarse-grid simulations that use Lagrangian particle tracking. Despite not being explicitly shown here, one can easily use our approach to construct models for Euler-Euler based simulations, as has been done recently by Igci et al. [1] or Parmentier et al. [4]. Our approach is universal, since it can be readily applied to cohesive and polydisperse systems. The main findings of our work can be summarized as follows:

- A fluid grid resolution of Δ_{fluid} / d_p between 3 and 6 was found to yield acceptable results for the domain-averaged slip velocity, which then varies less than 5% for particle volume fractions up to 0.25. For extremely dense flows, the requirement on the fluid grid resolution is even higher, and we recommend using a value for Δ_{fluid} / d_p less than 3.

- We observe cluster formation, leading to significant gas by-passing (see Figure 1), and consequently to a substantial increase in the dimensionless slip velocity (see Table 1). This gives evidence to the fact that cluster formation occurs even at scales smaller than previously reported [1].

- We propose a filtered drag law for coarse-grid Lagrangian-based simulations that is a function of the filtered particle volume fraction and dimensionless filter size. Our model is relatively insensitive to the microscopic drag model used, and hence we conclude that it reflects the effect of cluster formation on the flow, and not the features of a specific drag model.

- Lagrangian-based simulations also need to account for clustering in for cases in which the fluid grid resolution is larger than ca. 7 d_p, since conventional microscopic drag laws do not take this clustering into account.

Finally, it must be noted that the effective drag model presented here is only parameterized with the filtered particle volume fraction. This model cannot reflect the influence of the filtered slip velocity on the effective drag coefficient, which we observed when comparing results for systems with different $<\phi_p>$. The construction of a more precise model that takes this effect into account is underway.

REFERENCES

[1]   Y. Igci and S. Sundaresan: Constitutive Models for Filtered Two-Fluid Models of Fluidized Gas-Particle Flows. *Industrial & Engineering Chemistry Research*, 50 (2011), 13190-13201.

[2]   K. Agrawal, P.N. Loezos, M. Syamlal, and S. Sundaresan: The role of meso-scale structures in rapid gas–solid flows. *Journal of Fluid Mechanics*, 445 (2001), 151-185.

[3]   Y. Igci, A.T. Andrews, S. Sundaresan, S. Pannala, and T. O'Brien: Filtered Two-Fluid Models for Fluidized Gas-Particle Suspensions. *AIChE Journal*, 54 (2008), 1431-1448.

[4]   J.-F. Parmentier, O. Simonin, and O. Delsart: A functional subgrid drift velocity model for filtered drag prediction in dense fluidized bed. *AIChE Journal*, 58 (2012), 1084-1098.

[5]   J.W. Wang and Y.N. Liu: EMMS-based Eulerian simulation on the hydrodynamics of a bubbling fluidized bed with FCC particles. *Powder Technology*, 197 (2010), 241-246.

[6]   G. Xu and J. Li: Analytical solution of the energy- minimization multi-scale model for gas — solid two-phase flow. *Chemical Engineering Science*, 53 (1998), 1349-1366.

[7]   L.M. Zou, Y.C. Guo, and C.K. Chan: Cluster-based drag coefficient model for simulating gas–solid flow in a fast-fluidized bed. *Chemical Engineering Science*, 63 (2008), 1052-1061.

[8]   E. Helland, H. Bournot, R. Occelli, and L. Tadrist: Drag reduction and cluster formation in a circulating fluidised bed. *Chemical Engineering Science*, 62 (2007), 148-158.

[9]   E. Helland, R. Occelli, and L. Tadrist: Numerical study of cluster and particle rebound effects in a circulating fluidised bed. *Chemical Engineering Science*, 60 (2005), 27-40.

[10]   M. Xu, W. Ge, and J. Li: A discrete particle model for particle–fluid flow with considerations of sub-grid structures. *Chemical Engineering Science*, 62 (2007), 2302-2308.

[11]   E. Helland, H. Bournot, R. Occelli, and L. Tadrist: Drag reduction and cluster formation in a circulating fluidised bed. *Chemical Engineering Science*, 62 (2007), 148 - 158.

[12]   N. N.: OpenFOAM 1.7.1 User Manual. (2010), 1-204.

[13]   S. Radl, C. Radeke, J.G. Khinast, and S. Sundaresan: Parcel-Based Approach for the Simulation of Gas-Particle Flows. in: 8th International Conference on CFD in Oil & Gas, Metallurgical and Process Industries, Trondheim, Norway. SINTEF/NTNU Trondheim, 2011 124 (1-10).

[14] Z.Y. Zhou, S.B. Kuang, K.W. Chu, and a. B. Yu: Discrete particle simulation of particle–fluid flow: model formulations and their applicability. *Journal of Fluid Mechanics*, 661 (2010), 482-510.

[15] S. Luding: Cohesive, frictional powders: contact models for tension. *Granular Matter*, 10 (2008), 235-246.

[16] C. Wen and Y. Yu: Mechanics of fluidization. *Chem. Eng. Prog. Symp. Ser.*, 62 (1966), 100-111.

[17] R. Beetstra, M.A.V.D. Hoef, and J.A.M. Kuipers: Drag Force of Intermediate Reynolds Number Flow Past Mono- and Bidisperse Arrays of Spheres. *AIChE Journal*, 53 (2007), 489-501.

[18] S.H.L. Kriebitzsch, M. a. van der Hoef, and J. a. M. Kuipers: Drag force in discrete particle Models - Continuum scale or single particle scale? *AIChE Journal*, (in press) (2012), 1-9.

[19] A. Hölzer and M. Sommerfeld: Lattice Boltzmann simulations to determine drag, lift and torque acting on non-spherical particles. *Computers & Fluids*, 38 (2009), 572-589.

[20] S. Tenneti, R. Garg, and S. Subramaniam: Drag law for monodisperse gas–solid systems using particle-resolved direct numerical simulation of flow past fixed assemblies of spheres. *International Journal of Multiphase Flow*, 37 (2011), 1072-1092.

[21] C. Radeke, B.J. Glasser, and J.G. Khinast: Large-scale powder mixer simulations using massively parallel GPU architectures. *Chemical Engineering Science*, 65 (2010), 6435-6442.

[22] R. Issa: Solution of the Implicity Discretised Fluid Flow Equations by Operator Splitting. *Journal of Computational Physics*, 62 (1985), 40-65.

[23] H. Nilsson: PhD course in CFD with OpenSource Software. (2011), (http://www.tfd.chalmers.se/~hani/kurser/OS_CFD/).

[24] F.P. Kaerrholm: Numerical Modelling of Diesel Spray Injection, Turbulence Interaction and Combustion. Chalmers University of Technology, 2008.

[25] J.H. Ferziger and M. Peric: Computational Methods for Fluid Dynamics. Berlin. Springer, 2002.

[26] N.G. Deen, M. von Sint Annaland, and J.A.M. Kuipers: Multi-scale modeling of dispersed gas–liquid two-phase flow. *Chemical Engineering Science*, 59 (2004), 1853-1861.

[27] S. Radl and S. Sundaresan: Predictive Capabilities of a Parcel-Based Method for Dense Particle Flows. *Journal of Computational Physics*, submitted (2012), 1-63.

APPENDIX A - DETAILS OF THE NUMERICAL METHOD

A.1 Particle Phase

To advance the particle positions and velocities in time, we use an implementation based on the work of Radeke [21], with some modifications with respect to tangential contact forces and rolling friction [13]. To increase the robustness of the algorithm for fluid-particle flows, we take the gas-particle coupling force implicitly into account when updating the particle velocity $\mathbf{v}$. Thus, we obtain the particle velocities $\mathbf{v}_i$ at the new time step n+1 by setting:

$$\mathbf{v}_i^{(n+1)} = \frac{\mathbf{v}_i^{(n)} + \Delta t \left[\beta_{p,i} / \rho_p \, \mathbf{u}_i + \mathbf{g} - \nabla p_f / \rho_p + \mathbf{f}_{cont} / \left(V_{p,i} \, \rho_p \right) \right]}{1 + \Delta t \, \beta_{p,i} / \rho_p} . \tag{12}$$

A.2 Fluid Phase

For the fluid phase, we use a combination of the PISO (Pressure-Implicit with Splitting of Operators) scheme and the SIMPLE (Semi-Implicit method for Pressure-Linked Equation) scheme, which is termed PIMPLE here. Details of the implementation of these algorithms for single-phase flows can be found in the original work of Issa [22], as well in the publications of Nilsson [23], Kaerrholm [24], and Ferziger and Peric [25]. A new aspect for the present work is that we have to take (i) the displacement of fluid by the particles into account, and (ii) need to implicitly couple the two phases for stability reasons. The latter is critical for simulations of flows at high particle volume fractions and small particles sizes (i.e., large specific coupling forces $\boldsymbol{\Phi}$). We now focus on the handling of the velocity-pressure coupling and the handling of the coupling force. Therefore, we first rewrite the specific coupling force $\boldsymbol{\Phi}$ as:

$$\boldsymbol{\Phi}_j = \frac{1}{V_{cell,j}} \sum_{i \in V_{cell,j}} w_{ij} V_{p,i} \beta_{p,i} \left(\mathbf{v}_i - \mathbf{u}_i \right) . \tag{13}$$

Here i and j is the (fluid) cell and particle index, respectively. V_{cell} and w_{ij} is the volume of the fluid cell, and the weight of particle i in cell j (which is given by the mapping function, see below), respectively. To consider the fluid velocity field at time step n+1 (i.e., to consider the effect of the drag term on the fluid flow implicitly), we need to introduce the fluid velocity at the cell center ($\mathbf{u}^P_j$) in the coupling force term. This can be accomplished by a simple re-arrangement of the coupling force term:

$$\boldsymbol{\Phi}_j = \frac{1}{V_{cell,j}} \sum_{i \in V_{cell,j}} w_{ij} V_{p,i} \beta_{p,i} \left(\mathbf{v}_i - \left\{ \mathbf{u}_i - \mathbf{u}^P_j \right\} \right) - \frac{\mathbf{u}^P_j}{V_{cell,j}} \sum_{i \in V_{cell,j}} w_{ij} V_{p,i} \beta_{p,i} . \tag{14}$$

Thus, the first part on the right hand side of above equation is only weakly dependent on the fluid flow field (since the difference between $\mathbf{u}_i$ and $\mathbf{u}^P_j$ is small, and $\beta_{p,i}$ is a relatively weak function of the particle's relative velocity). This term will be taken into account explicitly. The second part, however, is now linearly dependent on the fluid flow field (again, here it is assumed that $\beta_{p,i}$ is a weak function of the particle's relative velocity). We are now in the position to write-down the discretized momentum equation for the fluid phase, where the coupling term is treated implicitly:

$$\left(a^{\mathbf{u}}_P + F_{coupl} \right) \mathbf{u}^P + \sum_N a^{\mathbf{u}}_N \mathbf{u}^N = -\phi_f \nabla p_{dyn} + \mathbf{r} . \tag{15}$$

Here a_P^u and a_N^u are the diagonal and off-diagonal coefficients in the system of algebraic equations, respectively. These vectors are obtained during the discretization of the momentum equation, by considering the local particle volume fraction. The latter is known from mapping the particle volumes to the Eulerian grid. The vectors $\mathbf{u}^P$ and $\mathbf{u}^N$ are the velocity vectors at the cell center P and at the neighboring cells, respectively. The vector $\mathbf{r}$ incorporates the known part of the system, i.e., the first term on the right hand side of the coupling force $\mathbf{\Phi}$, as well as the divergence of the viscous tensor. F_{coupl} is the coupling strength associated with the implicit part of the coupling term (see Eqn. 14). Based on Eqn. 15, an estimate for the new fluid velocity field can be calculated:

$$\mathbf{u}^P = \left(a_P^{\mathbf{u}} + F_{coupl} \right)^{-1} \left[\mathbf{H} - \phi_f \nabla p_{dyn} \right], \tag{16}$$

with

$$\mathbf{H} = \mathbf{r} - \sum_N a_N^{\mathbf{u}} \mathbf{u}^N . \tag{17}$$

By multiplication with ϕ_f and enforcing continuity (i.e., Eqn. 1), we obtain the following expression for the pressure:

$$\nabla \cdot \left[\rho_f \phi_f^2 \left(a_P^{\mathbf{u}} + F_{coupl} \right)^{-1} \nabla p_{dyn} \right] = \nabla \cdot \left[\rho_f \phi_f \left(a_P^{\mathbf{u}} + F_{coupl} \right)^{-1} \mathbf{H} \right] + \frac{\partial \left(\rho_f \phi_f \right)}{\partial t} . \tag{18}$$

In this equation the right-hand side is known from the previous calculation steps, and the resulting Poisson-like equation can be solved for the unknown dynamic pressure p_{dyn}. For this purpose we use fast geometric-algebraic multi-grid (GAMG) solvers with preconditioning [12]. Finally, the velocity $\mathbf{u}^P$ can be calculated using Eqn. 16 with the newly updated pressure.

A.3   Mapping

While the method of interpolation of Eulerian quantities (i.e., the pressure gradient and the fluid velocity) at the particle position has little influence on our results (we use tri-linear interpolation), the mapping of Lagrangian quantities to the Eulerian grid requires more attention. Same as in our previous work on bubbly flows, we use a 4th-order smoothing function [26] to calculate the weight w_{ij} of particle i in the fluid cell j. For the smoothing length we use the particle radius, such that particle volume and the fluid-particle interaction forces are distributed over the region occupied by the particle.

A.4   Numerical Settings

The particle contact force model requires us to specify a characteristic stiffness k_n, a damping coefficient γ_n and a friction coefficient. We have based these parameters on a characteristic dimensionless shear rate $\gamma^* = \left(u_t d_p / g \right) / \sqrt{k_n / \left(d_p \rho_p \right)} = 10^{-3}$, and the expression for the coefficient of restitution $e_p = \exp\left(-\gamma_n \pi / \sqrt{4 k_n / \left(m_{12} - \gamma_n^2 \right)} \right) = 0.90$. Here m_{12} is the reduced mass of the particles in contact, and u_t is the terminal settling velocity of an isolated particle. The time step was then chosen to be 1/50 of the contact time $t_c = \pi / \sqrt{k_n / m_{12} - \gamma_n^2 / \left(2 m_{12} \right)^2}$. These settings ensure that the particles are stiff enough to mimic hard spheres (i.e., quasi-static flow in dense regions and inertia-dominated flow in dilute regions [27]), as well as yield acceptably large particle time steps. We have chosen a value for the particle-particle friction coefficient

of $\mu_{PP} = 0.1$, and the tangential stiffness and damping coefficient were set to $k_t = 2/7 \ k_n$ and $\gamma_t = \gamma_n$, respectively.

To ensure a precise solution of the Navier-Stokes equation for the fluid phase, we perform six "pressure-velocity" correction loops (i.e., "outer corrections") and two pressure iterations (i.e., "inner corrections") within the PIMPLE algorithm. The relaxation factors for all but the last correction loop are 0.6 and 0.3 for the fluid velocity and pressure, respectively. We use second-order accurate spatial (central-differences-based) and temporal (a backward-Euler) discretization schemes. For the linear solvers (i.e., the solver for the Poisson-like pressure equation and the ones used to estimate the fluid velocity) we used absolute tolerances between 10^{-5} and 10^{-9} - these settings yielded stable simulations and acceptable mass conservation errors. The fluid time step was chosen such that the Courant number was below 0.3.